Optimal UAV Flights for Seeability and Endurance in Winds

A THESIS

SUBMITTED TO THE FACULTY OF THE GRADUATE SCHOOL

OF THE UNIVERSITY OF MINNESOTA

BY

Wei Guo

IN PARTIAL FULFILLMENT OF THE REQUIREMENTS

FOR THE DEGREE OF

MASTER OF SCIENCE

Yiyuan J. Zhao, Advisor

William L. Garrard, Co-Advisor

December, 2010

Acknowledgements

First, I give thanks to my adviser, Professor Yiyuan Zhao, not only for his wisdom and guidance but also for his support, encouragement and unending patience with me. Through him, not only have I learned knowledge and engineering skills in trajectory optimization, but also become a better writer and overall thinker. He has strengthened my understanding of how to research effectively, provided me with instructions on how I might proceed deeper and guided me many future research directions.

I also thank my co-advisor, Professor William Garrard, and Professor Rajesh Rajamani for taking the time to be the members of my thesis committee. As they are both experts in sensor technologies and control systems, I am eager to hear their responses to my work.

I am grateful to my parents, Weiping Guo and Guihua Wang, who have always been supportive and understanding, even when research has reduced the frequency of contact with them. Any success that I have today could not have been possible without them.

I also owe thanks to my friends, Heming Chen who always offer me technician support

unweariedly, and Zhefeng Li, Qian Zheng, Zhiqing Xing, Di Wu, Zhaodan Kong for their helpful advice and comments in my thesis and presentation.

This work is supported in part by the Navy under STTR through Mosaic ATM, Inc., under Project # 00009476, monitored by Marc Steinberg. I thank Stephen Pledgie at Mosaic ATM for many helpful discussions.

Dedication

This is dedicated to my parents.

ABSTRACT

Video-equipped unmanned aerial vehicles (UAVs) are highly useful in missions of surveillance, monitoring, and sensing. In these flights, the UAVs must maintain the ability to see the targets as well as to save energy for prolonged endurance. This paper examines basic patterns of UAV flights that can maximize its ability to "see" targets or seeability and/or minimize power consumptions to assist UAV mission planning. In this paper, a point-mass model is used to describe UAV motions. A seeability model is established that peaks when the UAV is flying at a certain angle from the normal vector perpendicular to the surface of the target. UAV flights are formulated as nonlinear periodic optimal control problems. The performance indices are selected to maximize the average seeability, to minimize the average power consumption, or to achieve a balance of the two. Motion constraints due to UAV performance capabilities and safety are imposed. The effects of different levels of constant wind velocities are considered. These nonlinear optimal control problems are converted into parameter optimization for numerical solutions. Extensive numerical solutions are obtained for UAV level flights with constant airspeeds and variable airspeeds, as well as three-dimensional flights. Clear tradeoffs between maximum seeability and minimum power are established.

Contents

List of Tables

List of Figures

List of Symbols

C_L	Lift coefficient
C_D	Drag coefficient
C_{D_0}	Zero-lift drag coefficient
D	Aerodynamic drag
d_c	Normalizing quantity for distance
$E_{\max}$	Maximum lift-to-drag ratio or aerodynamic efficiency
g	Gravitational acceleration
h	Altitude
h_{cr}	Critical altitude
I	Performance index
K	Induced drag factor
$(K_f, K_s.K_t)$	Weighting on (average power, average seeability, time) in cost functional
L	Aerodynamic lift
m	Aircraft mass

N	Number of nodes in the discretization of time interval
n	Load factor
P	Power
R	Distance of UAV from the target
r	Radius of A circular orbit
S	Vehicle reference area
$\mathbf{S}$	Seeability measure
T	Engine thrust
t	Time
V	Airspeed
V_c	Normalizing quantity for speed
(W_x, W_y, W_h)	Wind component along (East, North, Up)
(x, y)	(East, North) position coordinate
β	Wind force scale
θ	UAV viewing angle to target
θ_{op}	Optimal viewing angle
κ	Scaling factor in seeability measure
γ	Air-relative flight path angle
μ	Bank angle
Ψ	Heading angle measured clockwise from the North
ρ	Air density

τ	Normalized time
$\tilde{(\ )}$	Average of a variable
$\bar{(\ )}$	Normalized variable
$(\ )_0$	Initial value
$(\ )_f$	Final value
$\dot{(\ )}$	Time derivative
$(\ )'$	Derivative w.r.t. normalized time

Chapter 1

Introduction

Unmanned aerial vehicles (UAVs) are highly useful in missions of surveillance, detection, remote sensing, and monitoring. Often, these UAVs carry video equipment onboard to provide video information of an area and targets for human observers, and/or to provide visual clues for remote controls. In these missions, it is necessary that a UAV maintains or improves its ability to "see" the target while flying, or seeability.

The need to understand the performance of visual devices has long been recognized. The Johnson criteria[1], developed in 1951, describe both image- and frequency-domain approaches to analyzing the ability of observers to perform visual tasks using image intensifier technology. In this case, performance is defined in the sense of facilitating human decisions in the detection, orientation, recognition, and identification of target objects. Various studies on the subject has been continuing to this day[2–4]. However, little work has been found on the design of UAV flight trajectories to enhance their

ability to sense targets or to balance seeability and endurance.

Indeed, a UAV can position itself relative to a target in ways to achieve a desired level of seeability. Because air vehicles must keep moving in the air and cannot stay in one spot indefinitely in order to generate sufficient lift, the proper planning of flight trajectories for good "seeability" becomes important. In addition, these trajectories should not consume all the onboard powers of a UAV too rapidly. As a result, balancing the needs of seeability and energy efficiency in trajectory planning is desirable.

Furthermore, because UAVs are often light and small, they are highly prone to winds. This is especially true for UAVs employed for sensing missions. As a result, it is important, almost necessary to study their trajectory designs in the presence of winds. Example works that study optimal UAV flight patterns in winds for enhanced endurance can be found in Refs. 5-16. However, these works do not consider the need of good seeability in UAV flights.

This paper seeks to help lay a foundation in the design of UAV flight trajectories that balances the needs of seeability and endurance. It does so by studying the fundamental features of optimal UAV flight trajectories that maximize a measure of seeability, minimize the average power consumption for enhancing endurance, and/or achieve a desired tradeoff between the two considerations. The effects of different levels of constant winds on these optimal patterns and tradeoffs are also studied.

The organization of this paper is as follows: in Chapter 2, point-mass equations of motion are used to represent UAV motions and a seeability model is established

in Chapter 3. Chapter 4 formulates UAV flights in a specified region as nonlinear periodic optimal control problems. The performance indices are selected to maximize the average seeability, to minimize the average power consumption, or to achieve a balance of the two. Motion constraints are imposed to ensure physically feasible flights. These nonlinear optimal control problems are converted into parameter optimization for numerical solutions, and extensive numerical solutions are obtained. Chapter 5 demonstrates constant airspeed circular trajectories as reference trajectories to evaluate the benefits of optimal trajectories that are to be obtained. In Chapter 6, UAV level flights with constant airspeeds are first considered, followed by the studies of UAV level flights with variable airspeeds. Optimal three-dimensional UAV flights are then studied to examine the benefits of additional degrees of freedom in UAV motions. The effects of different levels of constant wind speeds on optimal UAV flights are also examined. Then, tradeoffs between seeability and power consumption are systematically examined. Main characteristics of these patterns and tradeoffs are summarized in Chapter 7.

Chapter 2

Equations of Motion for UAV Flights and Seeability Model

For trajectory optimization studies, UAV motions can be adequately represented by a point-mass model assuming flat earth[17−19]. The corresponding general 3-D point-mass equations of motion with all the wind terms are presented in Ref. 19. In this paper, it is assumed that the drag coefficient is modeled by the parabolic drag polar[20]

$$C_D = C_{D_0} + KC_L^2 \tag{2.1}$$

in which the induced drag factor K can be determined from the aerodynamic efficiency $E_{\max}$ and the zero-lift drag coefficient C_{D_0} as

$$K = \frac{1}{4E_{\max}^2 C_{D_0}} \tag{2.2}$$

In this paper, it is assumed that the wind velocity is constant and in the horizontal

plane. For periodic UAV motions, it can be further assumed that the wind field only has a component in the x-axis.

$$W_x = \beta V_c, \quad W_y = 0, \quad W_h = 0 \tag{2.3}$$

To obtain good numerical efficiency in the optimization process, the equations of motion are normalized. For a given characteristic speed V_c, define

$$\bar{V} = \frac{V}{V_c}, \quad (\bar{x}, \bar{y}, \bar{h}) = \frac{x, y, h}{V_c^2/g}, \quad \tau = \frac{t}{V_c/g}, \quad (\bar{T}, \bar{D}, \bar{L}) = \frac{T, D, L}{mg}, \quad \bar{P} = \frac{P}{mgV_c} \tag{2.4}$$

and

$$(\ )' = \frac{d(\ )}{d\tau} = \frac{V_c}{g}\frac{d(\ )}{dt} \tag{2.5}$$

Also define the normalized air density

$$\bar{\rho} = \frac{\rho V_c^2}{2(mg/S)} \tag{2.6}$$

where mg/S is wing loading. Thus

$$\bar{D} = \frac{1}{mg}\frac{1}{2}\rho V^2 S C_D = \frac{\rho S V_c^2}{2mg}\bar{V}^2 C_D = \bar{\rho}\bar{V}^2 C_D = \bar{\rho}\bar{V}^2(C_{D_0} + K C_L^2) \tag{2.7}$$

After some derivations, we obtain

$$\bar{V}' = \frac{\bar{P}}{\bar{V}} - \bar{\rho}\bar{V}^2(C_{D_0} + KC_L^2) - \sin\gamma \tag{2.8}$$

$$\Psi' = \bar{\rho}\bar{V}\frac{C_L \sin\mu}{\cos\gamma} \tag{2.9}$$

$$\gamma' = \bar{\rho}\bar{V}C_L\cos\mu - \frac{\cos\gamma}{\bar{V}} \tag{2.10}$$

$$\bar{h}' = \bar{V}\sin\gamma \tag{2.11}$$

$$\bar{x}' = \bar{V}\cos\gamma\sin\Psi + \beta \tag{2.12}$$

$$\bar{y}' = \bar{V}\cos\gamma\cos\Psi \tag{2.13}$$

In the above equations, trajectory state variables are $[\bar{V}, \Psi, \gamma, \bar{x}, \bar{y}, \bar{h}]$, and trajectory control variables are $[\bar{P}, C_L, \mu]$. Vehicle parameters include (C_{D_0}, K), and environmental parameters in these equations include $(\bar{\rho}, \beta)$.

2.1 Motion Constraints

UAV motions are subject to constraints due to vehicle performance capabilities and safety. These constraints can be expressed as bounds on states, controls, and/or their combinations.

Bounds on state variables include

$$\bar{V}_{\min} \le \bar{V} \le \bar{V}_{\max},\ \ \gamma_{\min} \le \gamma \le \gamma_{\max},\ \ \bar{h}_{\min} \le \bar{h} \le \bar{h}_{\max} \tag{2.14}$$

The minimum airspeed constraint is related to the stall limit, whereas the maximum airspeed bound is typically caused by vehicle structural limitations. Bounds on the

flight path angle reflect limitations on vehicle attitude from both mission requirements and vehicle performance. The altitude constraints represent terrain limitation, ceiling, or mission requirements.

In comparison, bounds on control variables include

$$\bar{P}_{\min} \le \bar{P} \le \bar{P}_{\max}, C_{L_{\min}} \le C_L \le C_{L_{\max}}, -\mu_{\max} \le \mu \le \mu_{\max} \tag{2.15}$$

where the bound values are discussed together with vehicle performance parameters below.

Furthermore, path constraints are generally needed due to bound on the load factor and seeability. The load factor is defined as

$$n = \frac{L}{mg} = \bar{\rho}\bar{V}^2 C_L \le n_{\max} \quad \text{or} \quad \bar{V}^2 C_L \le \frac{n_{\max}}{\bar{\rho}} \tag{2.16}$$

and a minimum requirement on a seeability measure at all times

$$0 \le \mathbf{S}_{\min} \le \mathbf{S} \le 1 \tag{2.17}$$

where a seeability model is discussed below.

Finally, bounds on control rates may also be imposed.

$$|\bar{P}'| \le (\bar{P}')_{\max}, \quad |C_L'| \le (C_L')_{\max}, \quad |\mu'| \le (\mu')_{\max}, \tag{2.18}$$

The above normalized equations and the constraints suggest that fundamental parameters for UAV flights in winds for seeability and endurance include

$$\bar{P}_{\min}, \bar{P}_{\max}, C_{L_{\max}}, C_{D_0}, E_{\max}, \bar{\rho}, \beta, \mathbf{S}_{\min}, n_{\max}, \mu_{\max} \tag{2.19}$$

2.2 Point-Mass Equations in Level Flight

Level flights for surveillance and monitoring offer operational simplicity. Under the assumptions of level flight in a constant wind field with zero vertical wind component

$$\gamma = 0 \quad \Rightarrow \quad \gamma' = \bar{\rho}\bar{V}C_L \cos\mu - \frac{1}{\bar{V}} = 0 \tag{2.20}$$

We have

$$C_L = \frac{1}{\bar{\rho}\bar{V}^2 \cos\mu} \leq C_{L_{\max}} \tag{2.21}$$

The simplified equations become

$$\bar{V}' = \frac{\bar{P}}{\bar{V}} - \bar{D} = \frac{\bar{P}}{\bar{V}} - \bar{\rho}\bar{V}^2(C_{D_0} + KC_L^2) \tag{2.22}$$

$$\Psi' = \frac{1}{\bar{V}} \tan\mu \tag{2.23}$$

$$\bar{x}' = \bar{V}\sin\Psi + \beta \tag{2.24}$$

$$\bar{y}' = \bar{V}\cos\Psi \tag{2.25}$$

In this case,

$$n = \bar{\rho}\bar{V}^2 C_L = \frac{1}{\cos\mu} \tag{2.26}$$

thus

$$|\mu| \leq \cos^{-1}\left(\frac{1}{n_{\max}}\right) \tag{2.27}$$

If it is further assumed that the speed is constant, Eq. (2.22) becomes an algebraic equation

$$\bar{P} = \bar{D}\bar{V} = \bar{\rho}\bar{V}^3(C_{D_0} + KC_L^2) = \bar{\rho}C_{D_0}\bar{V}^3 + \frac{K}{\bar{\rho}}\frac{1}{\bar{V}\cos^2\mu} \tag{2.28}$$

2.3 UAV Model Parameters

In the examples presented below, the following UAV parameters are used reflective of the ScanEagle UAV: $E_{\max} = 14$,$C_{D_0} = 0.04$, $\frac{W}{S} = 5$ lb/ft^2, $\frac{P_{\min}}{mg} = 0.001$ HP/lb, $\frac{P_{\max}}{mg} = 0.06$ HP/lb, and $\mathbf{S}_{\min} = 0.05$. The characteristic speed for normalization is selected to be $V_c = 200$ ft/s. The varying wind magnitudes are assumed to be within $\beta = 0 \sim 0.2$. The case of strong winds that can upset a UAV is not included in this paper.

In addition, some generic expressions are used for airspeed bounds as follows.

$$\bar{V}_{\min} = \frac{0.8}{\sqrt{\bar{\rho} C_{L_{\max}}}}, \quad \bar{V}_{\max} = \frac{1.5}{\sqrt{\bar{\rho} C_{L_{\rm cr}}}} \tag{2.29}$$

where $C_{L_{\rm cr}}$ is a typical cruise lift coefficient, such as corresponding to an angle of attack of 3-5 deg. Allowing for the transient nature of UAV flights, we assume that the maximum airspeed bound is 50% more than the typical cruise speed. Other parameters include

$$\begin{gathered} C_L = 0.0 \sim 1.2, \quad C_{L_{\rm cr}} = 2\pi(3^o \sim 5^o) = 0.329 \sim 0.548 \\ \mu_{\max} = 45^o, \quad \gamma_{\max} = 10^o, \quad n_{\max} = 4 \text{ g}, \quad h_{\max} = 15000 \text{ ft} \end{gathered} \tag{2.30}$$

and the control rate bounds are given by

$$\begin{aligned} \left(C_L'\right)_{\max} &= 0.3 \text{ (1.2/4 per second)} \\ \left(\mu'\right)_{\max} &= 0.1745 \text{ (10 degrees per second)} \\ \left(\bar{P}'\right)_{\max} &= 1.0 \text{ (100\% change in 1 seconds for propeller} - \text{driven)} \end{aligned} \tag{2.31}$$

Chapter 3

A Model of Seeability Measure

In general, seeability refers to the usefulness of information from optical sensors to human decision making and/or automated vehicle control. In this regard, a precise measure of seeability can be very complex and depends on a host of factors including terrain structure, scene illumination, target characteristics, design and operations of visual equipment, and UAV flight trajectories, as well as human operators' receptivity. Everything else being the same, flight trajectories can directly affect a UAV's ability to sense a target. To investigate fundamental features of UAV flights for optimal seeability, a simplified seeability model is developed in this paper that emphasizes the impact of flight trajectories.

Assuming a direct vertical sunlight, Figure 3.1 illustrates that the seeability depends on the distance of the UAV from the target point as well as the viewing angle. At a given altitude, identifying a target from directly above can be more difficult than at an offset

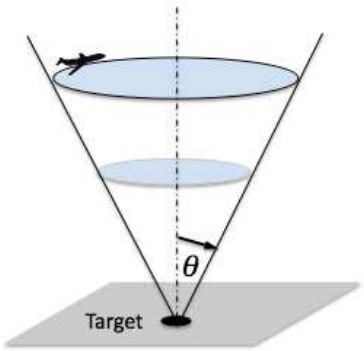

Figure 3.1: A seeability model.

angle. Instead, the best seeability is achieved when the vehicle is at a certain angle from the normal that is perpendicular to the surface. Along a cone of this optimal angle, a lower altitude improves the seeability and vice versa. On the other hand, it gets more difficult to view the target as the grazing angle becomes too shallow. In other words, seeability would be low directly overhead, reaches some maximum at moderate angles, and then approaches zero as the viewing angle approaches 90 degrees. Accordingly, a measure of seeability can be defined as

$$\mathbf{S} = \frac{\cos(\theta - \theta_{op})}{1 + \kappa(R/d_c)^2} \tag{3.1}$$

where θ_{op} is the optimal viewing angle, $d_c = V_c^2/g$ is the normalizing quantity for distance, and κ is a scaling factor. This definition indicates that a minimum distance ($R = 0$) from the camera at an optimal angle is chosen to be 100% seeable. The seeability then approaches zero asymptotically as the distance from the camera increases and as

the angle of incidence deviates more and more from the optimal angle. Naturally,

$$0 \leq \mathbf{S} \leq 1 \tag{3.2}$$

Assuming that the target is located at the origin: $x = 0, y = 0, h = 0$, we have

$$\bar{R} = \sqrt{\bar{x}^2 + \bar{y}^2 + \bar{h}^2}, \quad \cos\theta = \frac{\bar{h}}{\bar{R}}, \quad \sin\theta = \frac{\sqrt{\bar{x}^2 + \bar{y}^2}}{\bar{R}} \tag{3.3}$$

and

$$\mathbf{S}(\bar{x}, \bar{y}, \bar{h}) = \frac{\bar{h}\cos\theta_{op} + \sqrt{\bar{x}^2 + \bar{y}^2}\sin\theta_{op}}{\left[1 + \kappa(\bar{x}^2 + \bar{y}^2 + \bar{h}^2)\right]\sqrt{\bar{x}^2 + \bar{y}^2 + \bar{h}^2}} \tag{3.4}$$

In the current work, terrain is assumed flat and the effect of sun angle is omitted. In a more complex seeability model, the level of seeability would depend on the direction of sunlight. For example, viewing a target from downsun can be more difficult than when the sun is behind the camera. The seeability would depend on the viewing azimuth angle such that it is zero if the camera is between the sun and the target, and low when azimuth angles are around 180 degrees. Furthermore, viewing a target from low on the horizon in downsun is even more difficult than when higher. These additional factors can be considered in future work.

In addition, visual equipment such as a camera needs to be properly oriented in order to maximize exposure in sensing a target. This requires the coordination of trajectory planning with UAV attitude control so that the camera would face the target to the extent possible. In this case, a rigid-body model of UAV motions should be used. For simplicity, it is assumed that the cameras are mounted on a gimballed platform that can rotate. As a result, a point-mass model can be used to study optimal flight trajectories.

Chapter 4

Problem Formulation and Numerical Solution Methods

UAV flights over a specified target point are now formulated as a nonlinear periodic optimal control problem that seeks to optimize a certain performance index, subject to the UAV equations of motion, constraints discussed above, and boundary conditions for periodic flights. The performance indices are selected to minimize the average fuel consumption per cycle, to maximize the average seeability per cycle, or to achieve a certain tradeoff between the two. Fuel consumption for a propeller-driven UAV is directly related to its power. Since multiple period solutions can also satisfy boundaries conditions, a penalty on flight time is included. A generic performance index is stated

as

$$\begin{aligned}\min_{\bar{P},C_L,\mu;\tau_f} \quad I &= K_f\frac{1}{\tau_f}\int_0^{\tau_f}\bar{P}\;d\tau + K_t\tau_f - K_s\frac{1}{\tau_f}\int_0^{\tau_f}\mathbf{S}\;d\tau \\ &= K_f\tilde{\bar{P}} + K_t\tau_f - K_s\tilde{\mathbf{S}}\end{aligned} \tag{4.1}$$

where the final time τ_f is in general open. The open initial conditions include **some or all** of the initial states

$$\bar{V}(\tau_0) = \bar{V}_0, \Psi(\tau_0) = \Psi_0, \gamma(\tau_0) = \gamma_0, \bar{h}(\tau_0) = \bar{h}_0, \bar{x}(\tau_0) = \bar{x}_0, \bar{y}(\tau_0) = \bar{y}_0 \tag{4.2}$$

where $\gamma_0 = 0$ may be assumed for periodic trajectories. For closed periodic flights, **some or all** of the following terminal conditions are imposed

$$V(\tau_f) = \bar{V}_0, \Psi(\tau_f) = \Psi_0 + 2k\pi, \gamma(\tau_f) = \gamma_0 \tag{4.3}$$

where $k = 1, 0$ and

$$\bar{x}(\tau_f) = \bar{x}_0, \bar{y}(\tau_f) = \bar{y}_0, \bar{h}(\tau_f) = \bar{h}_0 \tag{4.4}$$

In theory, the periodic terminal constraint for the heading angle can be achieved either with $k = 0$ or $k = 1$. Numerically, different choices of k lead to different solution patterns, as we shall find out. Specifically, $k = 0$ produces a figure-eight flight pattern whereas $k = 1$ produces a nearly circular pattern.

The above optimal control problems are converted into parameter optimizations for numerical solutions. Over the last several decades, numerous numerical schemes have been developed to solve nonlinear optimal control problems[21−26]. Particularly, the conversion of optimal control problems into parameter optimization through a collocation

approach offers flexibility, simplicity, and computational speed, and is used here. In this approach, both state and control variables are approximately represented by their values at a series of discrete time nodes.

There are different ways of approximating the differential equations and path constraints in the conversion process. In this paper, differential equations are enforced as a system of nonlinear constraints through a forward difference scheme at the discrete time nodes[22]. Boundary conditions in Eqs. (4.2) - (4.4) are enforced as linear constraints, direct constraints on solution variables are enforced as variable bounds, and the upper limit on the load factor in Eq. (2.16) is treated as a nonlinear constraint. An example conversion process can be found in Ref. 11.

Converted parameter optimization problems are solved with the software program SNOPT[27]. Analytical gradient expressions are provided for the cost functions, whereas gradients of the nonlinear constraints are determined numerically. Equally spaced nodes are used and different numbers of nodes N are experimented. Results presented below are obtained with $N = 41$ for a balance among solution accuracy, convergence, and computational speed. The feasibility and optimality tolerance levels are selected as $\epsilon_f = 10^{-8}$ and $\epsilon_o = 10^{-6}$. A solution in most cases takes about 50 to 100 iterations. Initial guesses are based on an initial level circular trajectory at a constant speed.

Chapter 5

Reference Trajectory

Intuitively, circular level flight trajectories around a specified target would provide operational simplicity, and may be adjusted either to minimize the average power required or to maximize the average seeability. Therefore, constant airspeed circular trajectories are considered as reference trajectories to evaluate the benefits of optimal trajectories that are to be obtained.

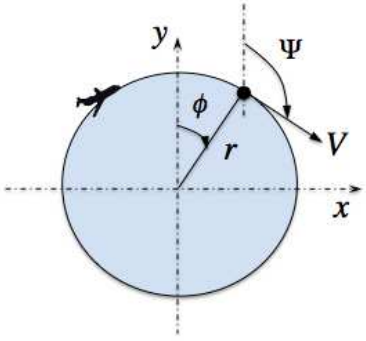

Figure 5.1: Level circular orbit.

Zero wind is assumed in establishing circular reference trajectories. As shown in Figure 5.1, the UAV flies in a circular orbit around the target with some constant airspeed, where $\phi = \Psi - 90^o$. From Eqs. (2.23) and (2.26), we have

$$\Psi' = \phi' = \frac{\bar{V}}{\bar{r}} = \frac{1}{\bar{V}} \tan \mu \tag{5.1}$$

or

$$\bar{r} = \frac{\bar{V}^2}{\tan \mu} = \frac{1}{\bar{\rho} \sin \mu C_L} \tag{5.2}$$

One can specify constant μ and C_L in order to define a circular orbit. The period of a circular orbit is given by

$$\tau_f = \frac{2\pi \bar{r}}{\bar{V}} \tag{5.3}$$

5.1 Minimum Power Circular Orbit

A constant speed level circular trajectory in zero wind is achieved with a constant bank angle. The optimal speed for minimum power flights with a constant bank angle can be determined from minimizing Eq. (2.28)

$$\min_{\bar{V}} \quad \bar{P} = \bar{\rho} C_{D_0} \bar{V}^3 + \frac{K}{\bar{\rho}} \frac{1}{\bar{V} \cos^2 \mu} \tag{5.4}$$

We have

$$\frac{\partial \bar{P}}{\partial \bar{V}} = 3\bar{\rho} C_{D_0} \bar{V}^2 - \frac{K}{\bar{\rho} \cos^2 \mu} \frac{1}{\bar{V}^2} = 0$$

or

$$\bar{V}^* = \left(\frac{K}{3C_{D_0}} \right)^{\frac{1}{4}} \frac{1}{\sqrt{\bar{\rho} \cos \mu}} \tag{5.5}$$

The corresponding minimum average power is given by

$$\bar{P}^* = \frac{4}{3}\frac{K}{\sqrt{\bar{\rho}}}\left(\frac{3C_{D_0}}{K}\right)^{\frac{1}{4}}\frac{1}{\cos^{1.5}\mu} \tag{5.6}$$

and the corresponding radius is given by

$$\bar{r}^* = \frac{1}{\bar{\rho}\sin\mu}\sqrt{\frac{K}{3C_{D_0}}} \tag{5.7}$$

Minimum power circular orbits would prefer the UAV to fly with as a small bank angle as possible with the corresponding optimal airspeed. A smaller bank angle results in a larger radius, which would run into constraints imposed on $\mathbf{S}_{\min}$ or the geometric constraints of the mission region.

5.2 Maximum Seeability Circular Orbit

A constant speed level circular trajectory at a specified altitude and radius defines a view angle. The optimal view angle for maximum seeability flights can be determined from

$$\max_{\theta} \quad \tilde{\mathbf{S}} = \frac{\cos(\theta - \theta_{op})}{1 + \kappa\bar{R}^2} = \frac{\cos(\theta - \theta_{op})\cos^2\theta}{\cos^2\theta + \kappa\bar{h}^2} \tag{5.8}$$

then mathematically, the optimal θ^* can simply be a function of the altitude. In this case, the radius of the orbit is determined accordingly. Constraints on μ and C_L in Eq. (2.21) limits the radius of the circle at the low altitude as follows,

$$\bar{r} \geq \frac{1}{\bar{\rho}\sin\mu_{\max}C_{L_{\max}}} \tag{5.9}$$

as will be confirmed below.

Chapter 6

Simulation

6.1 Optimal Level Flights with Constant Airspeeds

We first consider optimal UAV flights at a constant altitude with constant airspeed in zero wind conditions. These trajectories provide operational simplicity, and represent the limiting cases of three-dimensional trajectories under special conditions. In this case, the trajectory state variables include $(\Psi, \bar{x}, \bar{y})$, and the control variable is μ. The airspeed and period of an orbit trajectory $(\bar{V}, \tau_f)$ become control parameters. The optimization problem seeks to determine $(\mu(t), \bar{V}, \tau_f)$ to optimize the performance index in Eq. (4.1), where different choices of the weighting factors (K_f, K_s, K_t) may be used to obtain different types of optimal flights.

Figure 6.1 compares two basic patterns in the horizontal plane under zero wind for both minimum power and maximum seeability trajectories: one is a circular shape and

Table 6.1: Constant speed/flight time in 2-D level flight at h=1000 ft in zero wind

Case	Pattern	V ft/sec	t_f sec
min P	Circle	59.221	433.82
min P	Figure-8	59.267	388.62
max S	Circle	62.176	26.27
max S	Figure-8	63.415	54.70

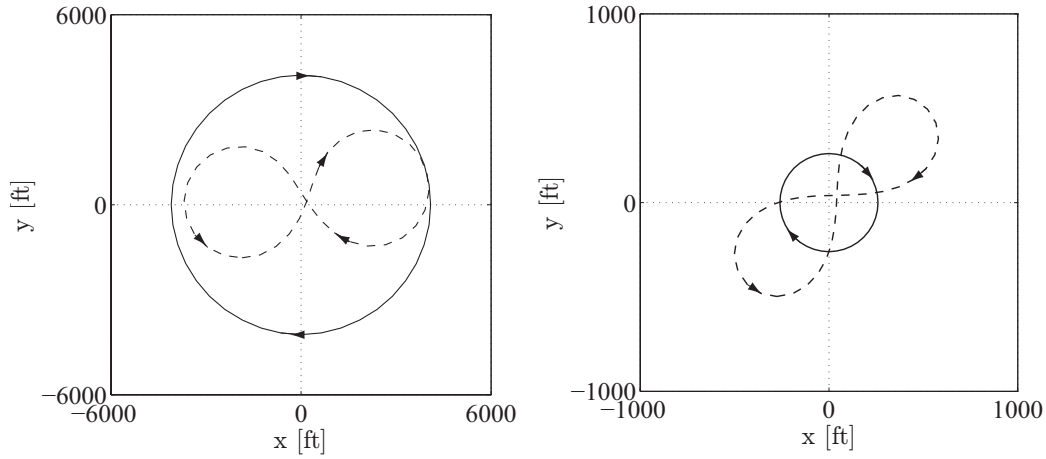

Figure 6.1: 2-D constant speed level flights at $h = 1000$ ft in zero wind: (a) minimum power (b) maximum seeability.

the other a figure-eight shape. For both the circular and the figure-eight patterns, the geometric dimensions of the maximum seeability trajectories are substantially smaller than those of the minimum power trajectories. This is to ensure that the vehicle always has a good view of the target point. For the minimum power flight, the circular pattern has a larger geometric dimension than the figure-eight pattern, whereas for the maximum seeability flight, it is the opposite. As shown in Table 6.1, the optimal constant airspeed is smaller for the minimum power flight, and is larger for the maximum seeability flight.

Figure 6.2 presents other trajectory variables for the minimum power trajectories.

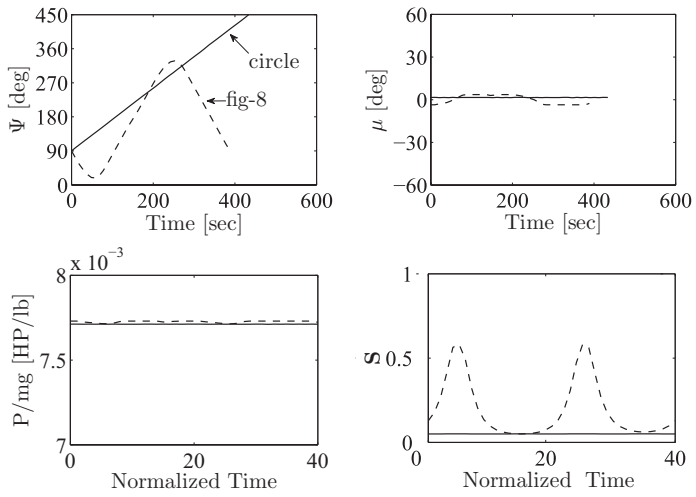

Figure 6.2: Trajectory variables for 2-D minimum power constant speed level flights in zero wind.

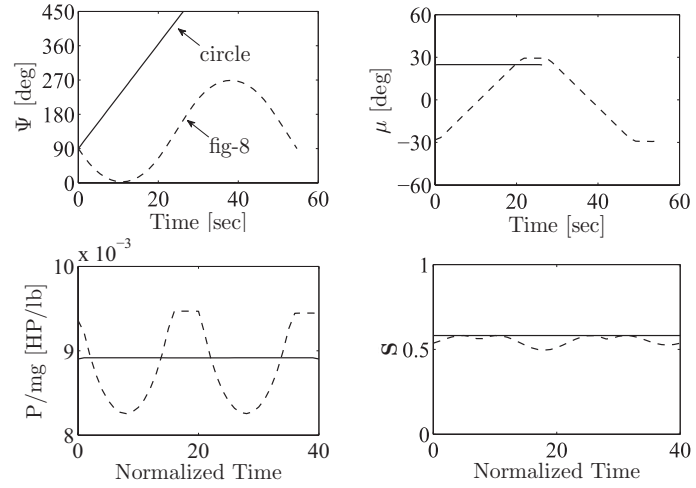

Figure 6.3: Trajectory variables for 2-D maximum seeability constant speed level flights in zero wind.

Here, the bank angle is very small corresponding to the small airspeed and a large flight radius. The minimum seeability constraint $\mathbf{S}_{\min}$ in Eq. (2.17) limits the maximum feasible radius in these flights, which in turn affects how small a bank angle is needed. The circular pattern with a smaller bank angle saves more power than that of the figure-eight pattern at the expense of reduced seeability. In comparison, Figure 6.3 presents other trajectory variables for the maximum seeability trajectories. The bank angle varies over a larger range than that for the minimum power trajectories; corresponding to the larger airspeed and smaller geometric dimension. Between the two patterns, the circular pattern achieves a better seeability level, which is the maximum seeability level of the figure-eight pattern over a trajectory period.

6.2 Optimal Level Flights with Variable Airspeeds

We now examine the effects of varying airspeed in level flights. It is expected that the additional degree of freedom introduced by varying airspeed may help to increase the level of optimality. In this case, the trajectory state variables include $(\bar{V}, \Psi, \bar{x}, \bar{y})$, and the trajectory control variables are $(\bar{P}, \mu)$. In addition, τ_f is the control parameter. The problem is again to optimize the performance index in Eq. (4.1) by varying both the control variables and the control parameter.

It turns out that in zero wind, optimal trajectories with airspeed as a state are the same as those with constant airspeed. In this section, further studies are made to examine effects of different trajectory parameters in level flights. In particular, the

effect of different altitudes is studied. It is found that the minimum power is almost the same in minimum power trajectories at different altitudes. In comparison, things are not so straightforward for the maximum seeability trajectories.

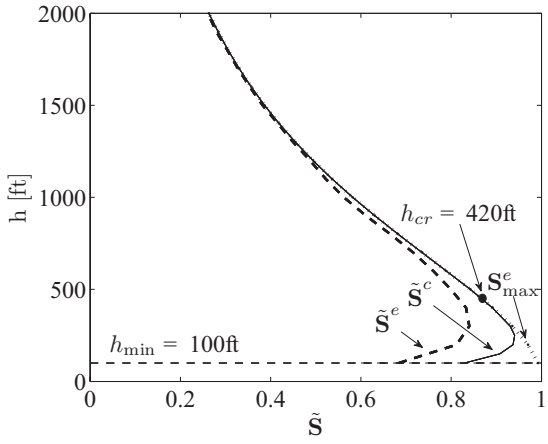

Figure 6.4: 2-D maximum seeability level flights at different altitudes.

Figure 6.4 demonstrates the seeability of two flight patterns in maximum seeability flights at different altitudes starting from $h = 100$ ft, where $\tilde{\mathbf{S}}^c$ and $\tilde{\mathbf{S}}^e$ denote the optimal average seeability achieved by the circular and figure-eight patterns, respectively. It is clear that both $\tilde{\mathbf{S}}^c$ and $\tilde{\mathbf{S}}^e$ change as altitude increases to a certain best level; beyond which they continuously decreases as altitude increases further. This is consistent with the seeability model used in this paper in Eq. (3.1). Below the best altitude, the numerator dominates the seeability, whereas beyond this altitude, further increase in altitude directly reduces seeability. Additionally, from Figure 6.4, $\tilde{\mathbf{S}}^c$ and $\tilde{\mathbf{S}}^e_{\max}$ essentially coincide except for those at $h \leq h_{cr}$, because $\tilde{\mathbf{S}}^c$ cannot attain its theoretically optimal value due to the constraints on μ and C_L in Eq. (5.9).

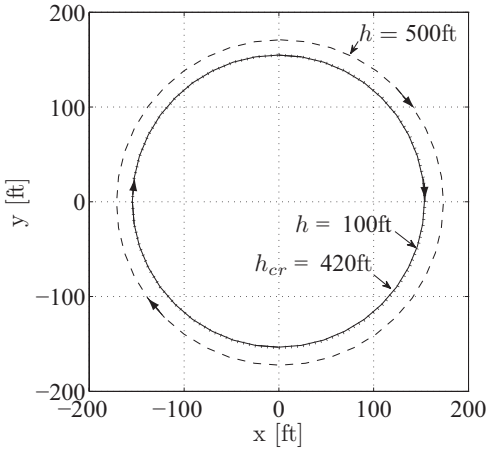

Figure 6.5: 2-D maximum seeability circular orbits at different altitudes.

For the maximum seeability level circular trajectories computed in this paper, $h_{cr} =$ 420 ft. Figure 6.5 illustrates that for $h > h_{cr}$, the radius of the circular orbit increases with the altitude. For $h \leq h_{cr}$, the radius does not decrease further as altitude decreases. It is worth noting that a different scaling factor κ in the definition of the seeability measure in Eq. (5.9) leads to a different h_{cr}, as shown in Figure 6.6. In other words, different κ represents different seeability measures. The smaller κ is, the more important the viewing angle to the seeability is; otherwise, the distance of the UAV from the target becomes more dominant.

Table 6.2: 2-D variable speed flight patterns at h=1000 ft in zero wind

Case	Circle/Fig-8	$\check{P}/mg, 10^{-3}$ HP/lb	$\check{\mathbf{S}}$
min P	$K_f = 1, K_s = 0$	7.712/7.726	0.0502/0.1979
combined	$K_f = 1, K_s = 0.01$	8.039/8.056	0.5594/0.4266
combined	$K_f = 1, K_s = 0.1$	8.354/8.605	0.5770/0.5514
combined	$K_f = 1, K_s = 1$	8.553/8.802	0.5790/0.5541
max S	$K_f = 0, K_s = 1$	8.916/8.905	0.5817/0.5581

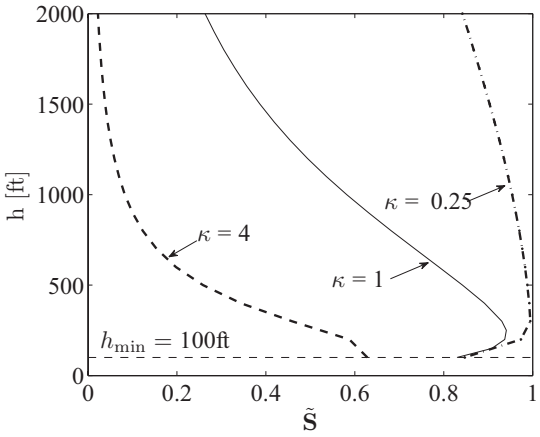

Figure 6.6: Effects of scaling factor κ in 2-D maximum seeability circular orbits at different altitudes.

We now examine the two patterns further. Table 6.2 summarizes the average normalized power and seeability in several typical cases of optimization performance indices under zero wind. Although the two patterns offer almost the same level of optimality in the minimum power and the maximum seeability flights, the overall performance of the figure-eight pattern falls behind those of the circular pattern, especially for the combined cases. We shall focus on studying the circular pattern and its variations subsequently.

Effects of winds on optimal flights are now studied. Figure 6.7 shows optimal airspeed profiles in level flights under two wind speeds ($\beta = 0.15$ and $\beta = 0.2$) for both the minimum power and the maximum seeability trajectories. In comparison, Figure 10 shows the optimal flight paths in the horizontal plane. The arrows represent the wind direction. The optimal airspeed basically stays constant for the minimum power flight in different wind conditions. For the maximum seeability flight, on the other hand, the

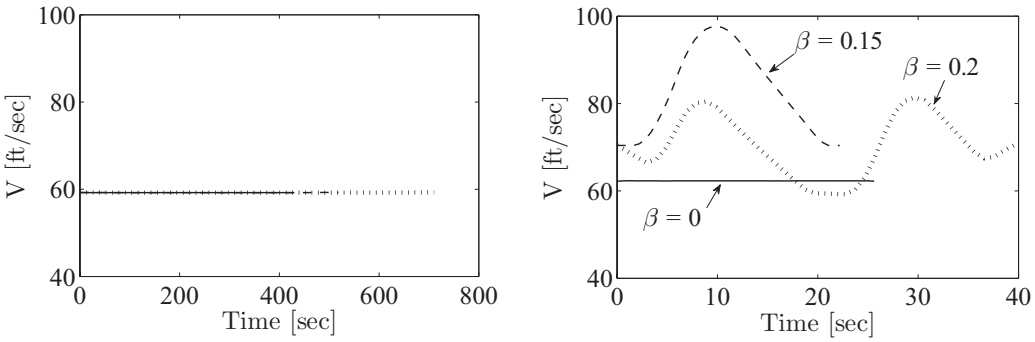

Figure 6.7: Airspeeds of 2-D variable speed flights in winds (a) minimum power (b) maximum seeability.

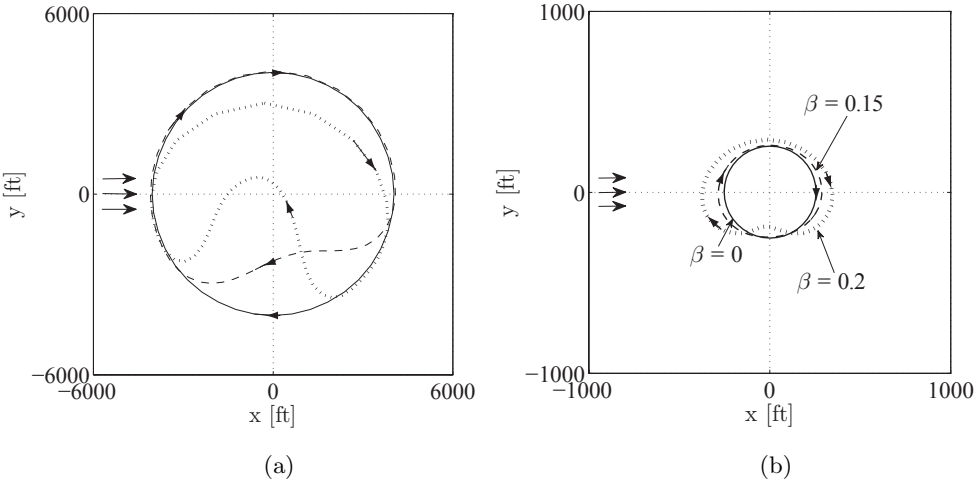

Figure 6.8: 2-D variable speed flight patterns in winds (a) minimum power (b) maximum seeability.

optimal airspeed profile varies significantly under different wind conditions in order to maintain sufficient seeability. As shown in Figure 6.8, shapes of the optimal trajectories deviate along the direction of the wind from the circular pattern as the wind increases. Stronger winds result in larger trajectory deviations.

6.3 Optimal 3-D UAV Flights

Finally, let us investigate optimal three-dimensional UAV flights by allowing vertical motions. It is expected that three-dimensional flights should bring additional benefits in terms of minimum power and/or maximum seeability than the level flights. Figure 6.9-6.12 illustrate characteristics of the optimal 3-D flights. These trajectories represent inclined and/or twisted circular patterns, and thus generalizations of the previous level flight optimal trajectories.

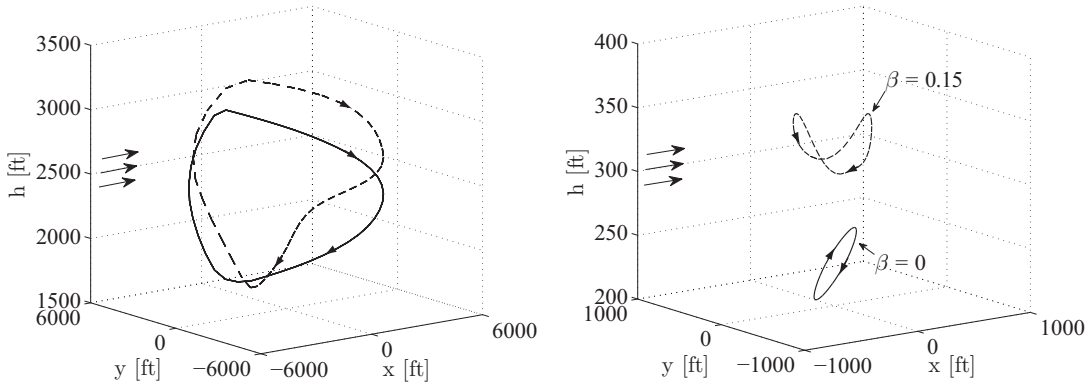

(a) (b)

Figure 6.9: 3-D flights in winds (a) minimum power (b) maximum seeability.

In the minimum power flight under zero wind (Figs. 6.9-6.11), the UAV climbs up

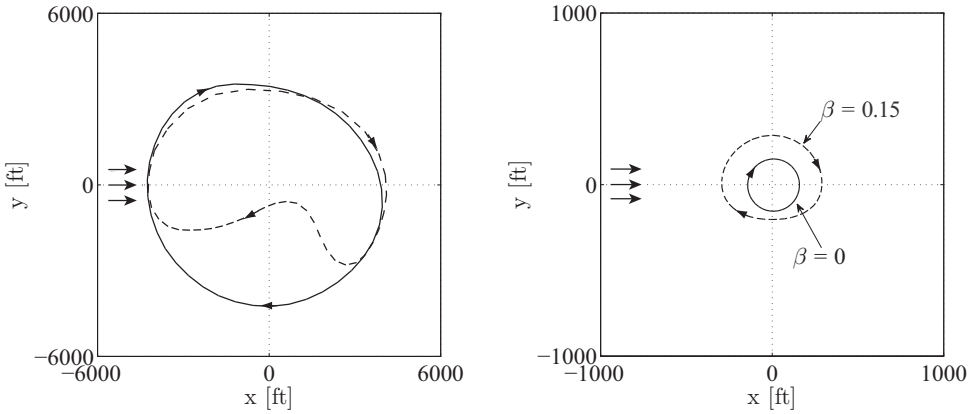

Figure 6.10: Top view of 3-D flights in winds (a) minimum power (b) maximum seeability.

rapidly and glide down over time with essentially constant airspeed. Power consumption occurs during the climb phase. The lift coefficient stays close to its maximum value during the entire flight, and the bank angle remains small. As wind increases, the airspeed still stays constant where the gliding time lasts longer. In comparison, the maximum seeability flight in zero wind (Figure 6.12) results in the periodic variations in both airspeed and altitude. A higher airspeed corresponds to a lower altitude; reflecting the exchange of potential and kinetic energies. The presence of winds increases the airspeed and prolongs the duration of the flight period. Accordingly, the flight altitude becomes higher in order to maintain seeability.

Figure 6.13 presents flight trajectories that seek a compromise between minimizing power and maximizing seeability. The presence of winds raises the altitude again, for the purpose of maintaining seeability.

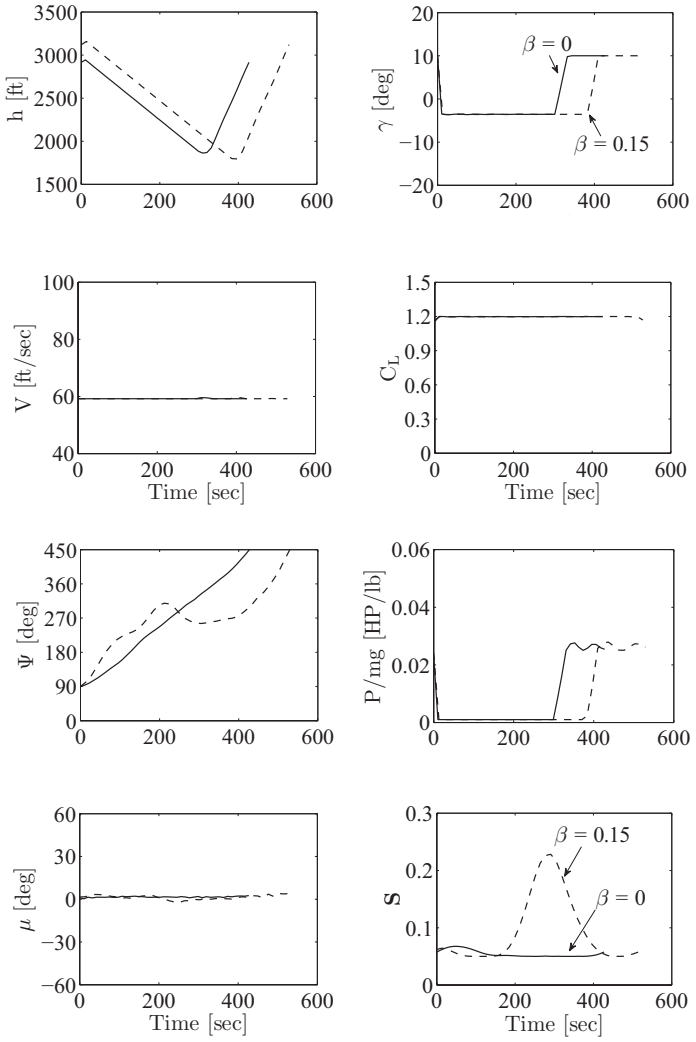

Figure 6.11: Trajectory properties of 3-D minimum power flights.

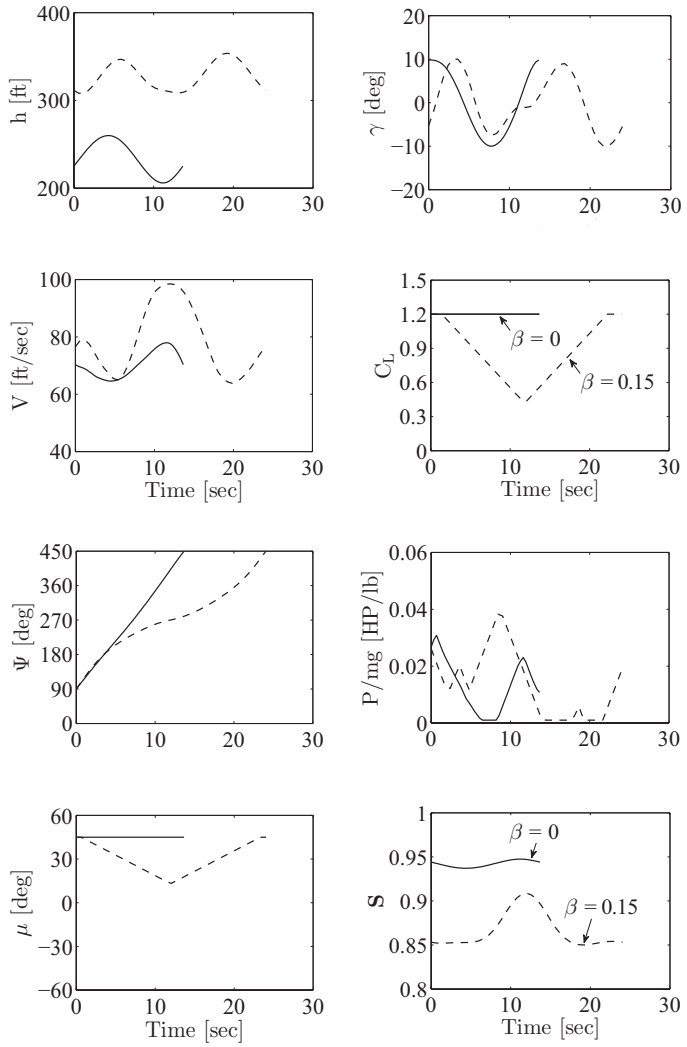

Figure 6.12: Trajectory properties of 3-D maximum seeability flights.

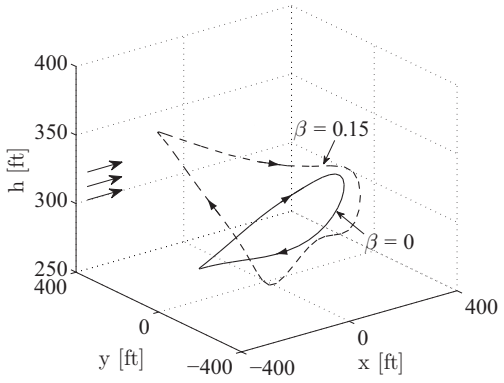

Figure 6.13: 3-D flights for combined power and seeability considerations: $K_f = 1$ and $K_s = 0.1$.

Table 6.3: Power-Seeability tradeoff in 3D fights

Case	$\beta = 0/\beta = 0.15$	$\tilde{P}/mg, 10^{-3}$ HP/lb	$\tilde{\mathbf{S}}$
min P	$K_f = 1, K_s = 0$	7.672/7.671	0.0545/0.0936
combined	$K_f = 1, K_s = 0.01$	8.094/7.950	0.7968/0.7020
combined	$K_f = 1, K_s = 0.1$	9.600/8.833	0.9040/0.8740
combined	$K_f = 1, K_s = 1$	13.05/8.894	0.9420/0.8746
max S	$K_f = 0, K_s = 1$	13.05/8.902	0.9421/0.8746

The effect of winds on power and seeability is summarized in Table 6.3. The presence of winds often causes the seeability to deteriorate, but helps to save power, particularly when the seeability concern is dominant in the optimization performance index for the combined cases. In particular, the wind field can help to significantly reduce the average power consumption when the maximum seeability is pursued. The comparison of Tables 6.3 and 6.2 indicate the superiority of 3-D flights over level flights in reducing power consumption and/or increasing seeability.

Figure 6.14 indicates that level flights are indeed special cases of 3-D flights under

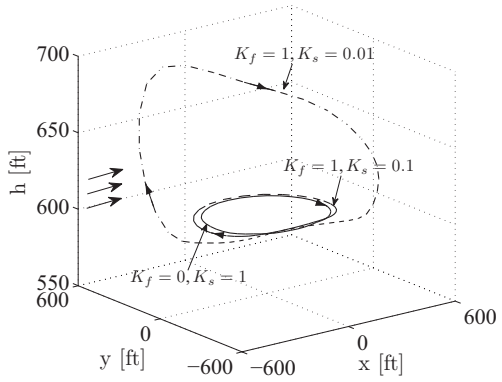

Figure 6.14: 3-D flights with altitude constraints ($\beta = 0.15$) at $h_{\min} = 600$ ft.

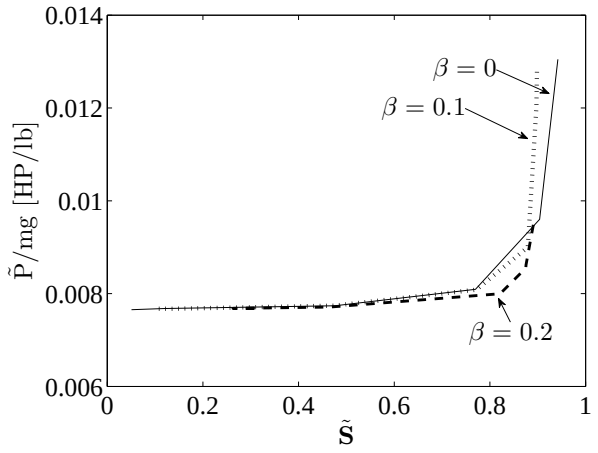

Figure 6.15: Power-seeability tradeoff in 3-D flights.

proper conditions. When a minimum flight altitude constraint $h_{\min}$ is imposed that exceeds the best flight altitude, optimal trajectories in winds for the seeability-dominated performance indices become level flights where the altitude stays at the lower bound of the altitude constraint. This is also true in zero wind conditions.

Finally, Figure 6.15 presents the tradeoff between the least required average power consumption and the desired average seeability in 3-D UAV flights. As the requirement on the desired average seeability increases, the least required average power increases. This increase is very gradually initially. As the desired average seeability exceeds a certain point, the corresponding required power starts to increase drastically. Clearly, a good operating point that balances the power consumption and seeability would be before this drastic increase. The presence of winds modify the exact values a little bit, but do not alter the trend.

Chapter 7

Conclusions

This paper examines basic patterns as well as tradeoffs in UAV flights that can maximize seeability and/or minimize power consumptions. In this paper, point-mass models are used to describe UAV motions. A seeability model is established that peaks when the UAV is flying at a certain angle from the normal vector perpendicular to the surface of the target. UAV flights are formulated as nonlinear periodic optimal control problems, and various motion constraints due to UAV performance capabilities are imposed. The effects of constant wind speeds are considered. Extensive numerical solutions are obtained for UAV level flights with constant airspeeds and variable airspeeds, as well as three-dimensional flights.

Clear patterns are identified for maximum seeability and minimum power flights. In constant speed level flights, two optimal flight patterns are possible depending on the terminal constraints: a circle pattern and a figure-eight pattern. In general, optimal

trajectories for maximum seeability flights have smaller spatial dimensions than those for minimum power flights. Further comparisons between the two patterns are made when airspeeds are allowed to vary in level flights, which show that the figure-eight pattern is a suboptimal solution in most cases. The circular pattern is then studied further. Results indicate that altitude is a significant factor to the level of seeability but not to power consumption. With the presence of winds, optimal trajectories for either minimizing power or maximizing seeability deviate from the basic circular pattern.

Three-dimensional flights offer additional savings in power consumption or enhancement in seeability compared with level flights. In particular, 3-D flights can utilize gliding motion to save power and/or search for favorable altitudes for seeability. In 3-D flights, the presence of wind is beneficial to additional power saving while it may reduce the level of seeability. If a minimum altitude constraint is imposed, 3-D optimal trajectories become level flights.

Finally, this paper establishes a clear tradeoff between the average power consumption and the average seeability. When the desired average seeability level is low, the vehicle can perform optimal flights that save the power consumption. As the desired average seeability increases, the least required power consumption increases, but initially very slowly. As the desired average seeability level increases beyond a certain point, the required power consumption starts to increase drastically. The presence of winds modifies the exact point at which required power starts to diverge, but does not fundamentally change this trend. Therefore, a good choice of the vehicle operating point

would be to impose a seeability requirement before the required average power diverges drastically.

Bibliography

1. Johnson, J., "Analysis of Image Forming Systems," *Image Intensifier Symposium*, Ft. Belvoir, VA., Oct. 6-7, 1958, AD 220160s (Warfare Electrical Engineering Department, U.S. Army Research and Development Laboratories), pp. 244-273.

2. Kopeika, N. S., *A System Engineering Approach to Imaging*, SPIE Press, 1998, pp. 337.

3. Vollmerhausen, R., and Robinson, A. L., "Modeling Target Acquisition Tasks Associated with Security and Surveillance," *Journal of Applied Optics*, Vol. 46, No. 20, 2007, pp. 4209-4221.

4. Morse, B., Engh, C., and Goodrich, M., "Aerial coverage maps for prioritized video searching,"Tech. Rep., Department of Computer Science, Brigham Young University, 2008.

5. Pierson, B. L., and De Jong, J. L., "Cross-Country Sailplane Flight as a Dynamic Optimization Problem," *Int. J. Num. Meth. Eng.*, Vol. 12, 1978, pp. 1743-1759.

6. Pierson, B. L., and Chen, I., "Minimum Landing-Approach Distance for a Sailplane," *J. Aircraft*, Vol. 16, 1979, pp. 287-288.

7. De Jong, J.L., "Instationary Dolphin Flight: The Optimal Energy Exchange Between a Sailplane and Vertical Currents in the Atmosphere," *Optimal Control Applications & Methods*, Vol. 6, 1985, pp. 113-124.

8. Lorenz, J., "Numerical Solution of the Minimum-Time Flight of a Glider Through a Thermal by Use of Multiple Shooting Methods," *Optimal Control Applications & Methods*, Vol. 6, 1985, pp. 125-140.

9. Jenkins, S. A., and Wasyl, J., "Optimization of Glides for Constant Wind Fields and Course Headings," *Journal of Aircraft*, Vol. 27, No. 7, 1990.

10. Bridges, P. D., "Alternative Solution to Optimum Gliding Velocity in a Steady Head Wind to Tail Wind," *Journal of Aircraft*, Vol. 27, No. 7, 1990.

11. Qi, Y. C., and Zhao, Y. J., "Energy-Efficient Trajectories of Unmanned Aerial Vehicles Flying Through Thermals," *Journal of Aerospace Engineering*, Vol. 18, No. 2, April 2005, pp. 84-92.

12. Metzger, D. E., and Hedrick, J. K., "Optimal Flight Paths for Soaring Flight," *J. of Aircraft*, Vol. 12, No. 11, Nov. 1975, pp. 867-871.

13. Sachs, G., Knoll, A., and Lesch, K., "Optimal Utilization of Wind Energy for Dynamic Soaring," *Technical Soaring*, Vol. 15, No. 2, 1991.

14. Zhao, Y. J., "Optimal Patterns of Glider Dynamic Soaring," *Optimal Control Applications and Methods*, Vol. 25, 2004, pp. 67-89.

15. Zhao, Y. J., and Qi , Y. C., "Minimum Fuel Powered Dynamic Soaring of Unmanned Aerial Vehicles Utilizing Wind Gradient," *Optimal Control Applications and Methods*, Vol. 25, 2004, pp. 211-233.

16. Zhao, Y. J., "Extracting Energy from Downdraft to Enhance Endurance of Uninhabited Aerial Vehicles," *Journal of Guidance, Control, and Dynamics*, Vol. 32, No. 4, July-August 2009, pp. 1124-1133.

17. Stengel, R. F., *Flight Dynamics*, Princeton University Press, 2004, Chaps. 2-3.

18. Vinh, N. X., *Optimal Trajectories in Atmospheric Flight* ,Elservier, Amsterdam, 1981, Chap. 3.

19. Jackson, M. R., Zhao, Y. J., and Slattery, R. A., "Sensitivity of Trajectory Prediction in Air Traffic Management," *Journal of Guidance, Control, and Dynamics*, Vol. 22, No. 2, 1999, pp. 219-228.

20. Anderson, J. D., Jr., *Introduction to Flight*, 5^{nd} ed., 2005, sec. 6.12, 6.13.

21. Betts, J., "Survey of numerical methods for trajectory optimization," *J. of Guidance, Control, and Dynamics*, Vol. 21, No. 2, pp. 193-207, 1998.

22. Hull, D. G., "Conversion of Optimal Control Problems Into Parameter Optimization Problems," *J. of Guidance, Control, and Dynamics*, Vol. 20, No. 1, pp.

57-60, 1997.

23. Fahroo, F., and Ross, I. M., "Direct Trajectory Optimization by a Chebyshev Pseudospectral Method," *J. of Guidance, Control, and Dynamics*, Vol. 25, No. 1, Jan. - Feb. 2002, pp. 160-166.

24. Gong, Q., Fahroo, F., and Ross, I. M., "A spectral algorithm for pseudospectral methods in optimal control," *Journal of Guidance, Control and Dynamics*, Vol. 31, No. 3, pp. 460-471, 2008.

25. Huntington, G.T. and Rao, A.V., "Optimal Reconfiguration of Spacecraft Formations Using the Gauss Pseudospectral Method," *Journal of Guidance, Control, and Dynamics*, Vol. 31, No. 3, March-April 2008, pp. 689-698.

26. Lu, P., "Use of Approximation Gradients in Trajectory Optimization," *Journal of Guidance, Control, and Dynamics*, Vol. 15, No. 5, 1992, pp. 1299-1301.

27. Gill, P. E., Murray, W., and Saunders, M. A. , "SNOPT: An SQP Algorithm for Large-Scale Constrained Optimization," Report NA 97-2, Dept. of Mathematics, Univ. of California, San Diego, and Report SOL 97-3, Dept. of EESOR, Stanford University, 1997.